Magnetic excitations and spin-Hamiltonian of the spin-5/2 distorted triangular lattice antiferromagnet Na$_3$Fe(PO$_4$)$_2$

B. Saha, A. K. Bera,[*] and S. M. Yusuf[†]

Solid State Physics Division, Bhabha Atomic Research Centre, Mumbai 400085, India
and Homi Bhabha National Institute, Anushaktinagar, Mumbai 400094, India

Roumita Roy and Sudipta Kanungo

School of Physical Sciences, Indian Institute of Technology Goa, Goa 403401, India

Duc Le and Aleksandra Krajewska

ISIS Facility, Science and Technology Facilities Council (STFC) Rutherford Appleton Laboratory,
Harwell Oxford, Didcot OX11 0QX, United Kingdom

We report magnetic ground state, dynamical magnetic properties, and the spin Hamiltonian of the two-dimensional distorted (J_1-J_2) triangular lattice antiferromagnetic (TLAFM) spin-5/2 system Na$_3$Fe(PO$_4$)$_2$ by neutron diffraction, inelastic neutron scattering (INS), and density-functional-theory (DFT) calculations. The compound Na$_3$Fe(PO$_4$)$_2$ is characterized by distorted triangular lattice with two different nearest neighbor exchange interactions J_1 and J_2; and having a collinear stripy antiferromagnetic (AFM) ground state. The powder INS spectrum consists of two bands of magnetic excitations (over 0.25–2.0 and 3.0–5.5 meV) with a small energy gap of ∼0.25 meV, a typical characteristic feature of spin-wave excitations of an ordered magnetic state. We model the experimentally observed features of magnetic excitations by linear spin-wave theory and determine the dominant in-plane magnetic exchange interactions $J_1 = -0.31$ meV (FM), and $J_2 = 0.15$ meV (AFM). The values of the exchange interaction constants determined from the INS study and the DFT calculations are in good agreement. Further, the interplanar exchange interaction [$J_3 = 0.00003$ meV (AFM)] has been estimated to be negligible. By determining the spin Hamiltonian through experimental INS and DFT calculations, we could shed light on the microscopic origin of the collinear stripy AFM ground state and verify the theoretical predicted magnetic phase diagram. Besides, the in-depth calculation of first principles Wannier function provides the exchange interaction mechanism between magnetic Fe ions in Na$_3$Fe(PO$_4$)$_2$. The present study provides an in-depth knowledge of magnetic ground state, their excitations and the spin-Hamiltonian of Na$_3$Fe(PO$_4$)$_2$ which is helpful to understand the phase diagram of a distorted TLAFM system in general.

I. INTRODUCTION

Understanding the exotic states of low dimensional magnetic systems, especially two-dimensional (2D) triangular lattice antiferromagnets (TLAFMs) is one of the major interests in current condensed matter physics. The TLAFMs are important for their numerous unusual magnetic properties, and subsequently they have gained significant attention in both theoretical and experimental research [1–4]. The competing magnetic exchange interactions in the TLAFMs lead to geometrical spin frustration and result in diverse magnetic ground states, such as noncollinear 120° chiral states, collinear AFM states, resonating valence bond states, and spin liquid states [5–10]. Uniform nearest neighbor (NN) AFM exchange interactions in TLAFMs [Fig. 1(a)] establish a 120° noncollinear chiral spin state [5–7,9,11], as

found experimentally in real compounds Ba$_3$MnSb$_2$O$_9$ [12], AFe(SO$_4$)$_2$ (A = Rb and Cs) [13,14], AFe(MoO$_4$)$_2$ (A = Rb, and Cs) [15,16], Rb$_4$Mn(MoO$_4$)$_3$ [17], Ba$_3$CoSb$_2$O$_9$ [18], Ba$_8$MnNb$_6$O$_{24}$ [19], *etc.* The TLAFM with unequal NN magnetic exchange interactions, which leads to a partial lifting of frustration, reveals significantly different magnetic states than the 120° noncollinear chiral spin state [20–24]. The variation in the exchange interaction values (J) of a triangular lattice leads to a surprisingly complicated and not yet fully understood phase diagram. Moreover, such magnetic phases show unconventional properties as a function of external perturbations like magnetic field and temperature.

The TLAFMs with unequal NN magnetic exchange interactions appear primarily due to the crystal structural distortions commonly observed in the real magnetic materials. The crystal structural distortions lead to unequal lengths of the sides of the triangular lattice, hence, different strengths of the exchange interactions. Recently, theoretical, and experimental efforts have tried to unearth the magnetic properties of the distorted TLAFMs [16,25–30]. Distorted TLAFMs can be of

---

[*]Contact author: akbera@barc.gov.in
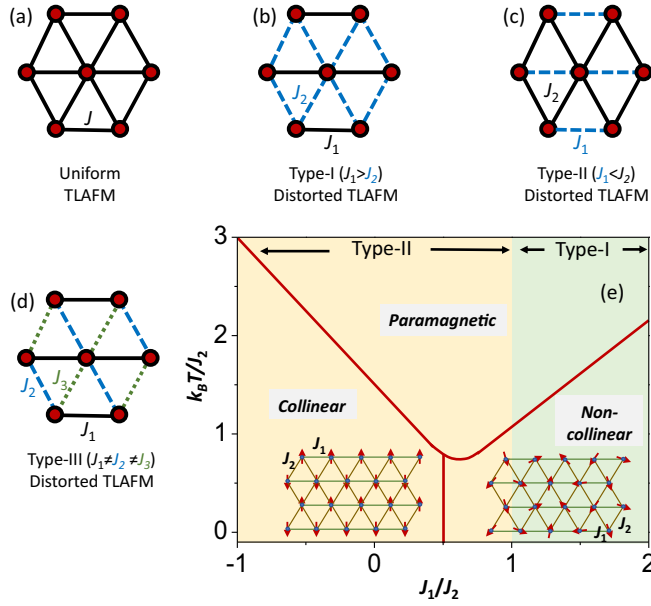[†]Contact author: smyusuf@barc.gov.in

FIG. 1. Variety of 2D triangular lattices, viz., (a) isotropic triangular lattice (with uniform exchange interactions J), and distorted triangular lattices of (b) type-I ($J_1 > J_2$), (c) type-II ($J_1 < J_2$) and (d) type-III ($J_1 \neq J_2 \neq J_3$). (e) Magnetic phase diagram for isosceles distorted triangular lattice [type-I ($J_1 > J_2$) and type-II ($J_1 < J_2$)], as reported in Ref. [30].

different types [Figs. 1(b)–1(d)], having either two different values of exchange interactions (for TLAFM with isosceles-type distortion) or three unequal exchange interactions (for TLAFM with scalene-type distortion). For the first category, i.e., with two different values of exchange interactions, there can be two different scenarios; (i) one strong exchange interaction J_1 and other two weaker exchange interactions J_2s (type-I), and (ii) two strong exchange interactions J_2s and one weak exchange interactions J_1 (type-II). The distorted TLAFMs with all unequal exchange interactions J_1, J_2, and J_3 can be labeled as type-III. First, we discuss the available theoretical results on such distorted TLAFM (isosceles-type distortion) systems. It is predicted that the nature of the magnetic ground state of a distorted TLAFMs is strongly dependent on the sign as well as the relative strength of these exchange interactions (J_1, J_2, and/or J_3) [25,26,28,30]. For the type-I ($J_1 > J_2$), when both J_1 and J_2 are AFM, the 120° noncollinear chiral state gets modified with the decreasing strength of J_2 (from the uniform case i.e., $J_2 = J_1$), leading to an incommensurate magnetic ordering for $J_1/J_2 > 1$ [25]. For the type-II ($J_1 < J_2$), when both J_1 and J_2 are AFM, the 120° noncollinear chiral state is stable down to $J_1/J_2 \sim 0.5$. With further lowering of the ratio J_1/J_2, a magnetic phase transition occurs to a collinear AFM state from the 120° noncollinear chiral state at $J_1/J_2 = 0.5$ [Fig. 1(e)] [30]. Further, with a FM J_1 and AFM J_2, the collinear AFM magnetic ground state remains stable for any value of J_1/J_2 for both types of the lattice distortion (type-I and type-II) [30]. On the other hand, there are no reports (as per our knowledge) for the type-III distorted TLAFMs with three nonequivalent NN exchange interactions.

Now we turn our attention to the experimental observations on such distorted TLAFM compounds. It is reported

that the strongly distorted TLAFM compound $Ag_3Cr(VO_4)_2$ having triangular lattices with one shorter (5.094 Å) and two longer (5.482 Å) sides (belongs to type-I) possesses a long-range collinear stripy AFM state in contrast to its undistorted counterpart $AAg_2Cr(VO_4)_2$ (A = Rb, K) with no long-range ordered magnetic ground state [29]. The weakly distorted triangular lattice of $Ca_3NiNb_2O_9$, belonging to the series $A_3NiNb_2O_9$ (A = Ba, Sr, and Ca) [27], is made of one shorter (5.4470 Å) and two longer (5.5056 Å) sides (belongs to type-I), and shows two magnetic phase transitions with varying temperature as compared to a single magnetic transition in the undistorted counterpart compound $Ba_3NiNb_2O_9$. Interestingly, the third compound $Sr_3NiNb_2O_9$ of this series belongs to type-II, having one longer (5.6387 Å) and two slightly shorter (5.6339 Å) sides, but also shows two magnetic phase transitions with varying temperature. Although the Ni^{2+} triangular lattice changes from an equilateral triangle (for A = Ba) into an isosceles triangle (for A = Sr and Ca), the noncollinear 120° antiferromagnetic state remains as the magnetic ground state for all the three compounds with A = Ba, Sr, and Ca, i.e., in the weakly distorted limit. However, the triangular lattice distortion effect is clearly demonstrated with the occurrence of the additional noncollinear magnetic phases (different from the 120° antiferromagnetic state) over the intermediate temperature region prior to setting up of the 120° antiferromagnetic state. Further, the weakly distorted TLAFM compound $Ba_3MnSb_2O_9$ with isosceles triangle (similar to $Sr_3NiNb_2O_9$) having one longer (5.881 Å) and two shorter (5.877 Å) sides (belongs to type-II) also depicts the noncollinear 120° antiferromagnetic state in the weak distortion limit [31]. Furthermore, the distorted triangular lattice compound $KFe(MoO_4)_2$ [16] (belongs to type-II) having two different kinds of layers shows the coexistence of both 120° noncollinear and collinear AFM orderings. The 120° noncollinear structure appears for the layers having triangular lattice with $J_1/J_2 > 0.5$. On the other hand, a collinear stripy AFM ground state appears for the triangular lattice layers having $J_1/J_2 < 0.5$.

It is, therefore, evident that different magnetic ground states can be possible for a distorted TLAFM depending on the relative strengths of the NN magnetic exchange interactions (J_1/J_2). Especially, the strongly distorted TLAFM having a collinear stripy AFM state is of special interest where several interesting magnetic properties are reported [32,33]. For example, despite of having 3D collinear stripy AFM ground state, coexistence of 3D and 1D spin-spin correlations were reported in the distorted TLAFM Cs_2CoBr_4 [33]. More interestingly, the application of magnetic field to such a distorted TLAFM with the collinear stripy AFM ground state leads to several phase transitions; first to a spin-density wave state, then to a collinear three sublattice up-up-down phase (resulting a 1/3- magnetization plateau), then to a paramagnet phase, and finally to a fully saturated phase [33]. Further, a coexistence of long-range and short-range spin-spin correlations, an indication of a magnetically inhomogeneous ground state, was reported for the distorted TLAFM $\alpha-NaMnO_2$ [34]. As per the theoretical phase diagram [Fig. 1], the collinear stripy AFM magnetic ground state in a distorted isosceles TLAFM can appear for two different conditions, viz., (i) for both AFM J_1 and J_2 exchange interactions or (ii)

for a FM J_1 and a AFM J_2 exchange interactions. Despite the same collinear stripy AFM ground state for above two cases, the temperature and magnetic field dependent properties are expected to be significantly different due to the different nature of NN exchange interactions. Hence, a thorough understanding of the spin Hamiltonian of distorted isosceles TLAFM having a collinear stripy AFM magnetic ground state is essential to shed light on their unusual magnetic properties; and need to be addressed further.

Our interest in the present study lies on the 2D distorted TLAFM $Na_3Fe(PO_4)_2$ with a collinear stripy AFM ground state. Recently, it was reported that the compound $Na_3Fe(PO_4)_2$ [35–38], belonging to the family of $Na_3R(AO_4)_2$ (where $R =$ Fe, Y, and $A =$ P, V, As, etc.) [39–42], shows a collinear stripy AFM spin state below ~ 10.6 K [38]. Now, for the compound $Na_3Fe(PO_4)_2$ with isosceles weak distorted triangular lattice, the side lengths of the triangles are almost equal [5.030 Å and 5.180 Å, respectively] with almost identical exchange interaction pathways through either Fe-O-P-O-Fe or Fe-O-O-Fe (Table II, and discussed later in detail). Therefore, from such structural features, almost equal strengths of the J_1 and J_2 exchange interactions may be expected. In contrast, for the observed collinear stripy AFM magnetic ground state in distorted TLAFM $Na_3Fe(PO_4)_2$, the ratio J_1/J_2 has to be either less than 0.5 (i.e., large difference in the J_1 and J_2 values) or negative (i.e., J_1 has be to FM). Hence, the knowledge of underlying spin Hamiltonian as well as the super exchange mechanisms in $Na_3Fe(PO_4)_2$ is essential to understand the true origin of the collinear stripy AFM ground state. The fingerprints of a spin Hamiltonian of a spin-system can be obtained from its characteristic energy-momentum relationships in the spin-excitations spectra. In this regard, inelastic neutron scattering (INS) serves as one of the main experimental tools, as it can access a broad range of wave vector and energy, enabling the observation and quantification of magnetic excitations over multiple Brillouin zones. Moreover, a recent NMR study on $Na_3Fe(PO_4)_2$ reported a two-magnon type spin dynamics and the presence of spin anisotropy gap of ~ 5.7 K (~ 0.49 meV) [35]. Although, some aspects of the low-temperature spin dynamical properties can be inferred from the NMR study, a direct determination of spin dynamical properties by a probe like inelastic neutron scattering and/or density functional theory (DFT) calculations is essential to determine the spin-Hamiltonian as well as spin-spin correlations. An INS study can provide much insight of spin-spin correlations in a distorted TLAFM system, as reported for the distorted TLAFM Cs_2MBr_4 ($M =$ Cu, Co) [33] where coexistence of 3D and 1D spin-spin correlations were established by INS.

In this paper, we have investigated the spin excitations of the 2D distorted TLAFM system $Na_3Fe(PO_4)_2$ by inelastic neutron scattering to address the origin of collinear stripy AFM magnetic ground state. In addition, a thorough characterization of the magnetic ground state of $Na_3Fe(PO_4)_2$ and its temperature and field dependences have been performed. The spin-Hamiltonian has been determined from experimentally measured INS spectra and its analysis by linear spin-wave theory. Besides, first-principles DFT calculations have been performed to corroborate the spin-Hamiltonian as well as to

reveal the exchange interaction mechanism. The experimental determination of the strengths of J_1 and J_2 allows us to shed light on the origin of the experimentally determined collinear stripy AFM state in $Na_3Fe(PO_4)_2$ as well as verification of the theoretical phase diagram with the distortion parameter J_1/J_2. In this paper, we divulge the microscopic origin of magnetic ground state by a combined INS and DFT studies, as well as establish the mechanism of exchange interactions which play an important role in the magnetism of distorted isosceles J_1-J_2 TLAFM in general.

II. EXPERIMENTAL DETAILS

A. Sample preparation and measurement techniques

Polycrystalline samples of $Na_3Fe(PO_4)_2$ (~ 20 gm) were synthesized by two-step solid-state reaction method [37]. Initially, $FePO_4$ was prepared by using the stoichiometric mixtures of high purity precursors Fe_2O_3 and $(NH_4)_2HPO_4$ at 1153 K for 72 h in air. The final compound $Na_3Fe(PO_4)_2$ was obtained by mixing the as-prepared $FePO_4$ with $(NH_4)_2HPO_4$ and Na_2CO_3 in a stoichiometric ratio, at 1013–1023 K in air for ~ 100 h.

The crystal structure of $Na_3Fe(PO_4)_2$ was investigated at room temperature by x-ray diffraction (using a laboratory-based source, Cu-K$_\alpha$ radiation), and neutron diffraction (using the powder diffractometer, PD-I ($\lambda = 1.094$ Å) at Dhruva Research Reactor, BARC, INDIA). The magnetic ground state structure was investigated by low temperature neutron diffraction [using the powder diffractometer, PD-II ($\lambda = 1.2443$ Å)] at Dhruva Research Reactor, Bhabha Atomic Research Centre, Mumbai, India. The measured diffraction patterns were analyzed by the Rietveld refinement technique using the FULLPROF computer program [43]. For the determination of the magnetic structure, the representation theory analysis [44] was performed using the BASIREPS software [43,45,46]. The dc-magnetization, ac-susceptibility, and heat capacity measurements were performed by a commercial Physical Properties Measurement System (Cryogenic Co. Ltd., UK).

The INS measurements on powder samples of $Na_3Fe(PO_4)_2$, were carried out using the time-of-flight spectrometer MAPS (for higher incident energy of $E_i = 20$ meV) and MARI (for lower incident energy of $E_i = 5$ and 2 meV) at the ISIS facility, Rutherford Appleton Laboratory, Didcot, United Kingdom. A total of ~ 20 gm powder samples were used for the INS measurements. The powder samples were loaded in a thin double-walled cylindrical aluminum (Al) can to make annular shaped powder samples. The can was then mounted into a helium gas based closed cycle refrigerator for the low temperature measurements. The $S(Q,w)$ time-of-flight data were plotted and analyzed (by suitable energy cuts and momentum cuts) by the "*Mslice*" program implemented in the "*Mantid*" software package [47]. The spin-wave simulations were performed using the "*SpinW*" computer program [48,49].

B. Theoretical DFT calculations

The DFT calculations were performed within the plane-wave basis set based on the pseudopotential framework as implemented in the Vienna ab-initio simulation

package (VASP) [50,51]. The generalized gradient approximation (GGA) exchange correlation function was employed following the Perdew-Burke-Ernzerhof prescription [52,53]. The experimentally obtained crystal structure was optimized by relaxing the atomic positions towards equilibrium until the Hellmann-Feynman force becomes less than 0.001 eV/Å, keeping the lattice parameters fixed at their experimentally obtained values. The correlation effects beyond the scope of GGA were taken into consideration by introducing the Hubbard U through GGA+U calculations [54,55] with suitable values of U_{eff} (U-J_H) at the Fe (5 eV) site. The calculations were performed with a plane wave cutoff of 500 eV and $6 \times 6 \times 4$ k mesh in the Brillouin zone for self-consistent calculations. In order to obtain the low energy Hamiltonian, *ab initio* derived Wannier function basis [56] using downfolding technique was acquired. Only the Fe-3d orbitals were kept as active degrees of freedom in constructing the low energy Hamiltonian while the rest were downfolded through a renormalization process, so that the resultant low energy Hamiltonian had the essence of the system as a whole.

III. RESULTS AND DISCUSSIONS

A. Crystal structure and magnetic ordering

$Na_3Fe(PO_4)_2$, belonging to the glaseritelike structural family of compounds, has a layered crystal structure. The magnetic layers are composed of corner sharing FeO_6 octahedra and PO_4 tetrahedra. Such magnetic layers are well separated by Na-ion layers along the crystallographic c axis by a distance ~6.91 Å (Fig. 2) [57]. The combined Rietveld analyses of the room temperature x-ray and neutron diffraction patterns [Figs. 2(a) and 2(b)] yield lattice parameters, $a = 9.059(7)$ Å, $b = 5.035(6)$ Å, $c = 13.823(6)$ Å, and $b = 91.48(3)°$ (space group: $C2/c$). The values of the lattice parameters are in good agreement with the previous reports [37,38]. The fractional position coordinates of the atoms are given in Table I. Within the magnetic layers in the ab plane, Fe^{3+} ($3d^5$, $S = 5/2$) ions form a distorted triangular lattice with two unequal Fe^{3+}-Fe^{3+} distances of 5.030(5) and 5.180(3) Å [Fig. 2(d)]. Our DFT calculation reveals that the dominating in-plane superexchange interactions J_1 (for the Fe-Fe distance: 5.030 Å) and J_2 (for the Fe-Fe distance: 5.180 Å) between the Fe ions occur via Fe-O-O-Fe pathways (Table II), without involving the contribution from P ions (discussed later in detail).

Our dc, ac-susceptibility, and heat capacity studies [Figs. 3(a), 3(b), and 3(c)] reveal a magnetic long-range ordering at ~10.8 K. The ordering temperature is in good agreement with the previous report [35,38]. Moreover, a broad peak at ~6 K in the heat capacity and the magnetization curve is visible. The broad peak could arise due to a short-range magnetic ordering of the "disordered" component of the net moment (as discussed later while describing the derived magnetic structure). An absence of hysteresis loop and remanent magnetizations in the M vs H curves down to 5 K indicates an AFM order [Fig. 3(d)]. The derivative of isothermal magnetization (dM/dH) [Fig. 3(d)] reveals a peak at ~32 kOe (for below $T_N = 10.8$ K), indicating a field induced spin-flop transition consistent with the earlier report [38].
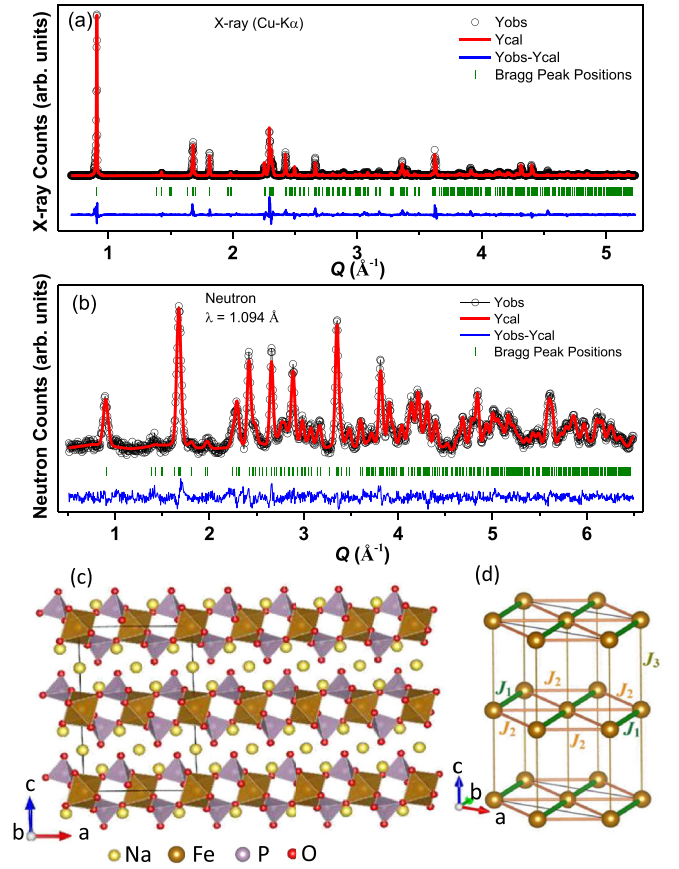

FIG. 2. Rietveld analyzed room temperature (a) x-ray and (b) neutron diffraction patterns for $Na_3Fe(PO_4)_2$. The observed and the calculated patterns are represented by black symbols and red solid lines, respectively. The blue lines represent the difference between the observed and calculated patterns. The vertical green bars represent the allowed Bragg peak positions. (c) The schematic layered crystal structure of $Na_3Fe(PO_4)_2$. (d) The possible nonuniform in-plane exchange interactions in $Na_3Fe(PO_4)$ having different Fe-Fe bond distances [green (J_1) and yellow (J_2) for in-plane exchange interactions and dark yellow (J_3) for interplanar exchange interaction]. For clarity, Na and P atoms are not shown.

Such a spin-flop transition indicates the presence of a weak magnetic anisotropy which is confirmed from our inelastic neutron scattering measurements (discussed later in detail). The magnetic phase diagram in the H-T plane [Fig. 3(e)]

TABLE I. Rietveld refined crystal structural parameters for $Na_3Fe(PO_4)_2$.

Atoms	Site	x/a	y/b	z/c	Occupancy
Fe	4a	0	0	0	0.5
P	8f	0.168(6)	0.514(8)	0.387(7)	1
Na1	4e	0.000(5)	0.027(7)	0.250(9)	0.5
Na2	8f	0.327(7)	0.053(6)	0.368(7)	1
O1	8f	0.106(8)	0.319(4)	0.465(6)	1
O2	8f	0.334(4)	0.590(9)	0.412(8)	1
O3	8f	0.081(9)	0.783(8)	0.386(8)	1
O4	8f	0.165(7)	0.384(5)	0.286(7)	1

TABLE II. Bond distances and the bond angles of the supersuperexchange pathways of the in-plane exchange interactions.

Exchange Interactions	Super-exchange Pathways	Bond Distances (Å)		Bond Angles (deg)	
J_1	Fe-O1-O3-Fe	Fe-O1	1.941(11)	Fe-O1-O3	144.6(6)
		O1-O3	2.588(14)	O1-O3-Fe	111.6(4)
		O3-Fe	2.065(11)		
J_2	Fe-O3- O2-Fe	Fe-O3	2.065(11)	Fe-O3-O2	116.1(6)
		O3-O2	2.513(15)	O3- O2-Fe	149.3(6)
		O2-Fe	1.962(10)		

(obtained from temperature dependent dc susceptibility and isothermal magnetization measurements) depicts three well defined regions corresponding to paramagnetic phase above ~ 10.8 K, an AFM state ($H < 32$ kOe), and spin-flop phase (above ~ 32 kOe) below the $T_N \sim 10.8$ K. The magnetic phase diagram in the H-T plane is in agreement with the earlier report [38]. In the present work, all three phases, viz., paramagnetic, AFM state and the spin-flop phases are reproduced for our sample.

The temperature dependent neutron diffraction patterns [Figs. 4(a), 4(b), and 4(e)] reveal magnetic Bragg peaks below ~ 11 K, corresponding to the commensurate AFM phase [Fig. 4(c)], characterized by $\boldsymbol{k} = (1, 0, 0)$ [35,38]. Each of the triangular planes is formed with antiferromagnetically coupled FM chains, known as the stripy AFM state. Such collinear AFM ground state may appear due to a strong distortion in the triangular lattice having significantly different NN AFM exchange interactions ($J_1/J_2 < 0.5$) or due to NN exchange interactions with different signs, i.e., FM

J_1 and AFM J_2 [58–62]. Our analysis reveals that the moments lie predominantly in the bc plane with the magnetic moment components $m_a = 0.29(9)\,\mu_B$, $m_b = 1.78(6)\,\mu_B$, and $m_c = 3.06(6)\,\mu_B$, having a net ordered magnetic value of $3.77(6)\,\mu_B/Fe^{3+}$ at 6 K [Fig. 4(f)]. The ordered moment value of $3.77\,\mu_B/Fe^{3+}$ is smaller than the theoretically expected value of $5\,\mu_B/Fe^{3+}$ for $S = 5/2$, nevertheless, it is in agreement with that $(4.0 - 4.4\,\mu_B/Fe^{3+})$ predicted by DFT calculation (discussed later). The reduced ordered moment value indicates that some part of the moment remains disordered. The moment component m_b changes sign in the alternating layers along the c axis, whereas, the moment components m_a and m_c remain unchanged [Fig. 4(c)]. It may be noticed that the magnetic structure in the earlier report [38] differs from the present study especially the change of the sign of the m_c component in Fig. 10(a) of Ref. [38]. The symmetry analyses that reported in Table I of Ref. [38] agree well with present analyses. Moreover, the reported irreducible representation Γ_3 which describes the magnetic structure and fits the experimental magnetic pattern also agrees with present analyses. Given the basis vector symmetries of Γ_3 (Table I of Ref. [38]), the change of sign is only allowed for the m_b component, i.e., along the b axis [as shown in Fig. 4(c)] which was wrongly plotted in Fig. 10(a) of Ref. [38]. To verify further, we have simulated the magnetic diffraction pattern considering the magnetic structure of Fig. 10(a) of Ref. [38] (antiparallel m_c component). The simulated pattern is shown in Fig. 4(d) of the revised manuscript in comparison with the experimental pattern. It is evident that the calculated diffraction pattern could not reproduce the experimental magnetic pattern. In the present manuscript, nevertheless, the magnetic structure is generated considering the correct spin alignments and is shown in Fig. 4(c).

With the increasing temperature, the ordered magnetic moments decrease and a small magnetic moment ($\sim 0.5\,\mu_B/Fe^{3+}$) persists at 11 K due to the presence of spin-spin correlations (short-range) above the $T_N = 10.8$ K [inset of Fig. 3(a)]. The temperature dependent neutron diffraction patterns depict a broad diffuse magnetic peak above the T_N and persists up to 15 K [Fig. 4(e)], a signature of short-range spin-spin correlations. Additionally, the temperature dependent dc susceptibility data also exhibits a broad peak centered around ~ 15 K [inset of Fig. 3(a)] supporting the presence of short-range magnetic correlations. Here, we would like to mention that the collinear AFM phase as determined from the neutron diffraction study is used for the spin-wave calculations of the INS spectra.
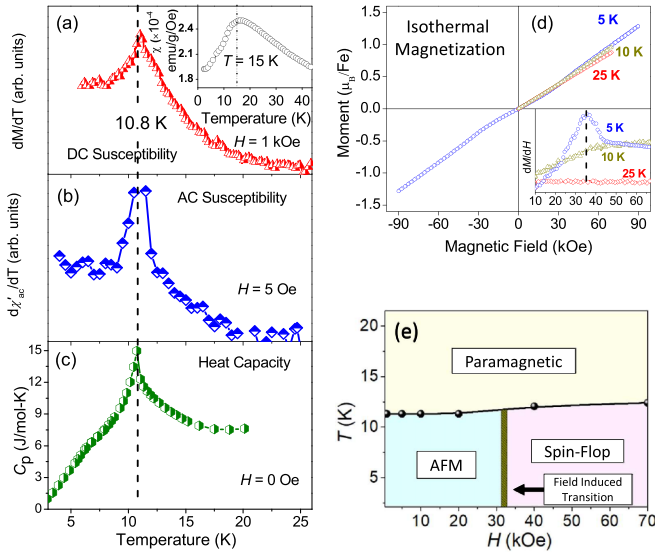

FIG. 3. Temperature derivative of (a) dc magnetization (dM/dT) and (b) ac susceptibility ($d\chi'_{ac}/dT$) curves as a function of temperature for $Na_3Fe(PO_4)_2$. The inset of (a) shows dc susceptibility (χ) as a function of temperature. (c) Heat capacity (C_p) as a function of temperature in zero applied field. (d) Isothermal magnetization curves measured at 5, 10, and 25 K. The inset shows field dependent derivative of magnetization (dM/dH). (f) Magnetic phase diagram of $Na_3Fe(PO_4)_2$ in the H-T plane.
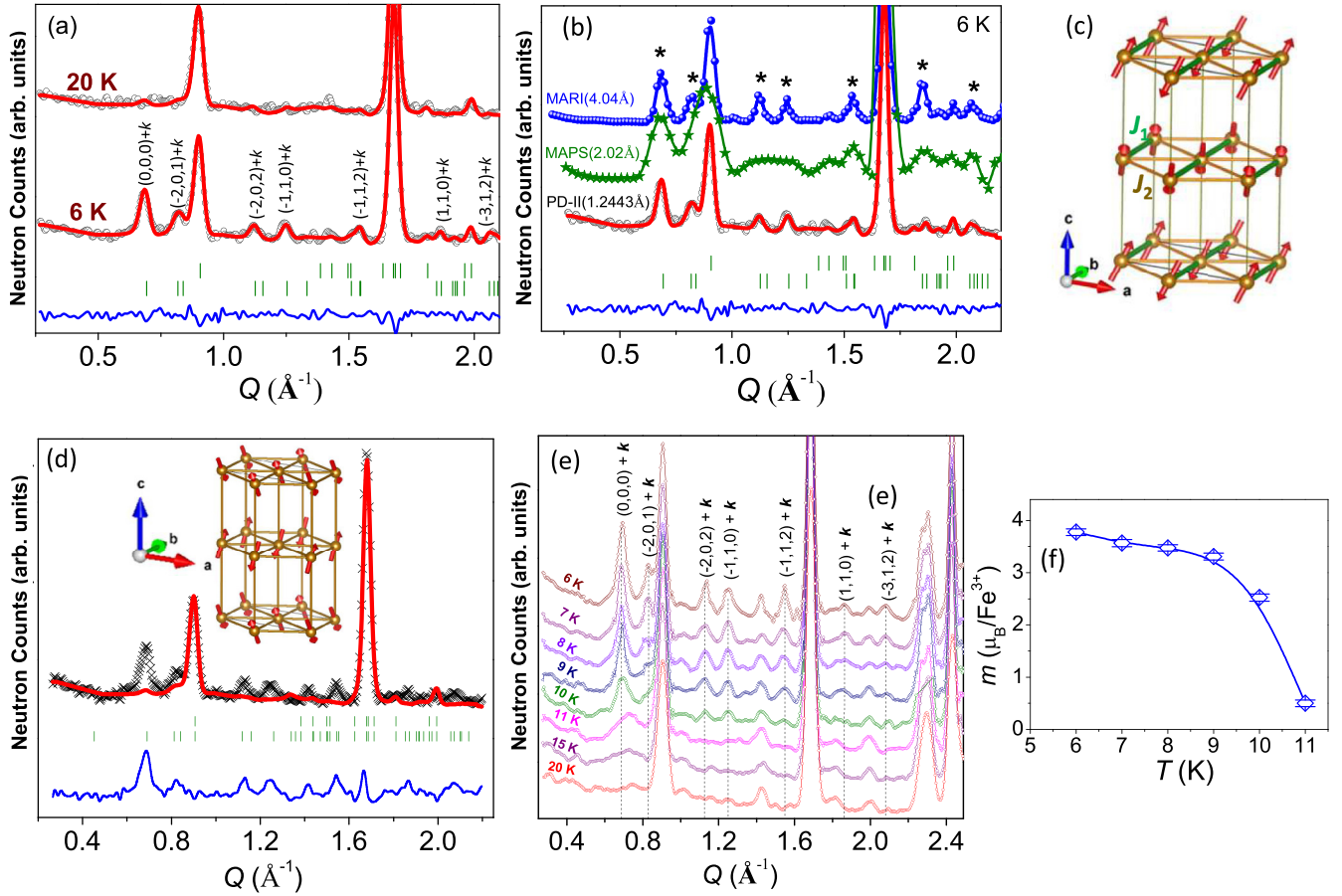
FIG. 4. (a) Rietveld analyzed neutron powder diffraction patterns at 20 K (paramagnetic state) and 6 K (AFM state) for $Na_3Fe(PO_4)_2$. The observed and the calculated patterns are represented by black symbols and red solid lines, respectively. The blue lines represent the difference between the observed and calculated patterns. The vertical bars represent the allowed nuclear Bragg peak positions (top row) and the allowed magnetic Bragg peak positions (bottom row). (b) Comparative neutron diffraction patterns obtained from MARI (blue), MAPS (green), and PD-II (black) instruments. (c) The schematic of collinear stripy AFM structure for $Na_3Fe(PO_4)_2$. (d) Rietveld analyzed neutron diffraction pattern with the magnetic structure reported in Ref. [38] having moment along the *bc* plane. Temperature-dependent (e) neutron diffraction patterns and (f) ordered magnetic moments of Fe^{3+}.

B. Magnetic excitations and spin-Hamiltonian (inelastic neutron scattering)

The magnetic excitation spectra of $Na_3Fe(PO_4)_2$ were measured by inelastic neutron scattering (INS) on powder samples at 6 K using the TOF spectrometers MAPS with incident neutron energy of $E_i = 20$ meV [Figs. 5(a) and 5(b)] and MARI with $E_i = 7$ meV, respectively [Fig. 5(d)]. Both the INS spectra reveal two bands of scatterings over ∼0.25–2.0 and 3.0–5.5 meV, respectively, whose intensity decreases with the increase of Q, indicating its magnetic origin. The magnetic origin of the excitation mode was further confirmed by a temperature dependent INS measurement on MAPS, where the absence of the mode was found at 240 K [Fig. 5(c)]. The variation of intensity of the excitation mode with energy has been estimated by an integration over $|Q|$ range of $0-3.5$ Å^{-1} [Figs. 5(c) and 5(f)], which shows the energy bands over ∼0.25–2.0 meV and 3.0–5.5 meV with peaks at ∼1.5 meV and ∼4.5 meV, respectively.

The high-resolution excitation spectrum from MARI with incident neutron energy $E_i = 2$ meV reveals a small en-

ergy gap of ∼0.25 meV at $Q = 0.75$ Å^{-1} [Figs. 5(e) and 5(g)] below the low energy magnetic excitation mode over 0.25–2.0 meV. The energy gap value shows reasonably good agreement with the spin anisotropy gap reported from the NMR study [35] possibly arising due to the presence of single ion anisotropy. The observed small energy gap of ∼0.25 meV at $Q = 0.75$ Å^{-1} [Figs. 5(e) and 5(f)] corresponds to a very weak single-ion anisotropy of $D \sim 0.02(2)$ meV (given in Table III), which is ∼6% of the strongest exchange interaction ($D/J_1 = 0.06$). Such an energy gap is also in agreement with the observed magnetic field induced spin-flop transition at $H_c = 32$ kOe [Fig. 3(d)]. According to a recent report, although no first-order single-ion anisotropy is expected for an Fe^{3+} ion ($3d^5$ electron configuration), the second-order perturbation between the magnetic ground and excited states can lead to a small single ion anisotropy via spin-orbit couplings [35]. The experimental inelastic neutron spectra contain characteristic features of the spin Hamiltonian. Despite losing directional-dependent information through powder averaging, the powder $S(|Q|, \omega)$ retains singularities originating from the
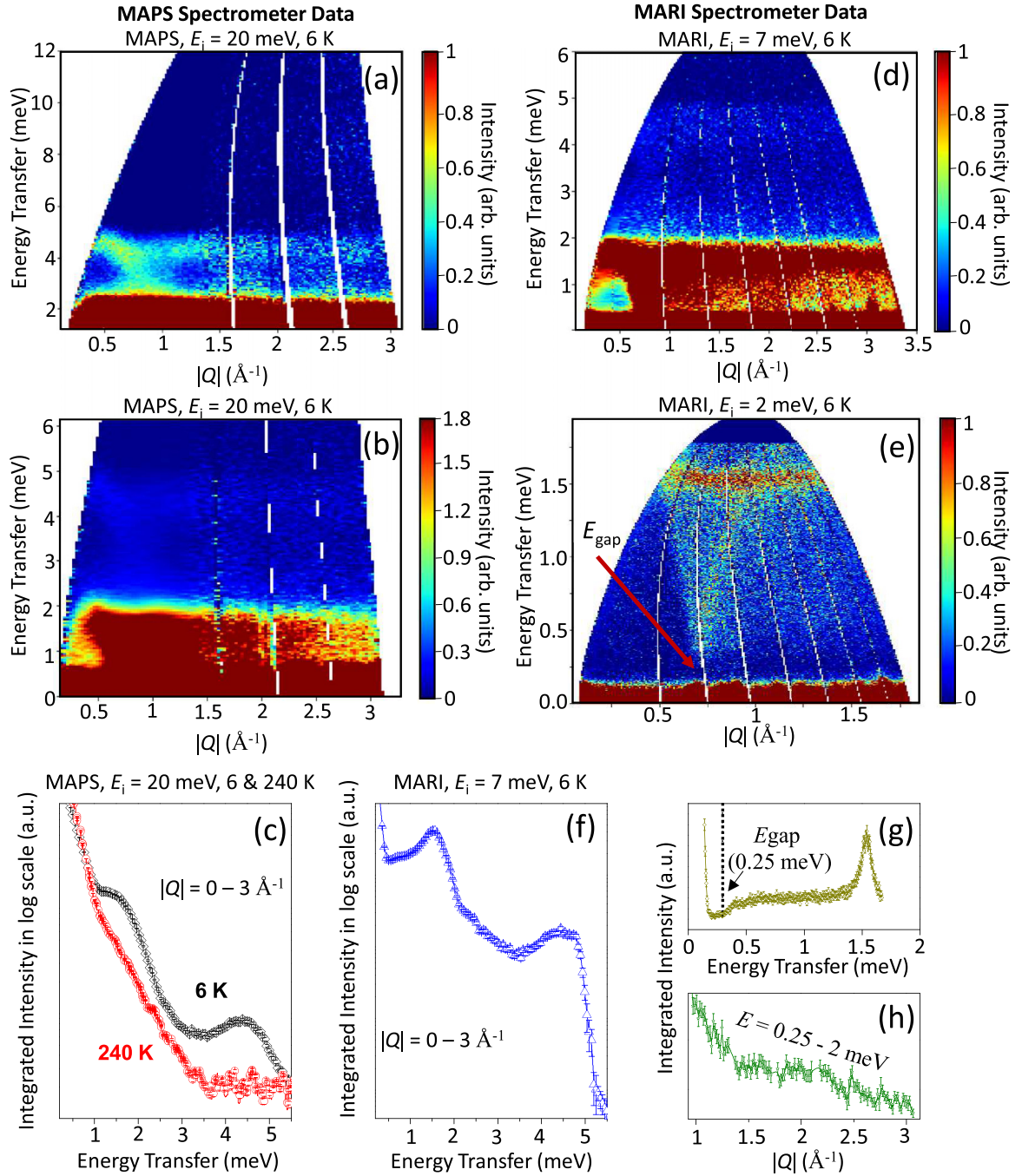
FIG. 5. 2D color map of the inelastic neutron spectra of $Na_3Fe(PO_4)_2$ measured using (a), (b) the MAPS spectrometer with $E_i = 20$ meV at 6 K. (d), (e) MARI spectrometer (at 6 K) with $E_i = 7$ and 2 meV, respectively. The color scales represent the scattering intensity in arbitrary units. Integrated intensity vs energy transfer curves obtained from (c) MAPS spectra for 6 K (black curve) and 240 K (red curve), and (f) MARI spectra for 6 K (revealing a band of magnetic excitation over 0.25–2.0 and 3.5–5.5 meV). (g) The constant Q cut [integrated over $|Q| = 0.6$–0.85 Å^{-1} of the spectrum in (e)] as a function of energy transfer, revealing an energy gap of 0.25 meV. (h) A constant energy cut [integrated over energy 0.25–2.0 meV of the spectrum in (d)] as a function of momentum transfer ($|Q|$).

density of states as a function of energy, and thus it provides unique characteristics of the spin-Hamiltonian to estimate the exchange interaction constant J parameters. The spin-Hamiltonian is determined by analyzing the experimental spectra using the linear spin-wave theory. We mention here that no noticeable contribution from phonon modes, is evident over the energy-momentum range of the measured spectra.

We have calculated the magnetic excitation spectra based on a model Hamiltonian [Fig. 2(d)] of $Na_3Fe(PO_4)_2$ by using the "*SpinW*" program, and the results are compared with the experimentally observed INS spectra. $Na_3Fe(PO_4)_2$ contains only Fe^{3+} ($3d^5$, $S = 5/2$) magnetic ions and therefore, we have considered interactions between Fe^{3+} ions only. Considering the 2D layered XXZ triangular lattice system, the

TABLE III. The exchange interaction values determined from the INS study and DFT calculations.

	Inelastic neutron scattering		
Exchange interactions	J_1 (meV)	J_2 (meV)	D (meV)
Value	$-0.31(1)$ (FM)	0.15(1) (AFM)	0.02(2)
	DFT calculations		
Interaction pathways	$U_{\mathrm{eff}}^{\mathrm{Fe}} = 4\,\mathrm{eV}$	$U_{\mathrm{eff}}^{\mathrm{Fe}} = 5\,\mathrm{eV}$	$U_{\mathrm{eff}}^{\mathrm{Fe}} = 6\,\mathrm{eV}$
J_1 (meV) Fe-Fe in plane	-0.41 FM	-0.33 FM	-0.26 FM
J_2 (meV) Fe-Fe in plane	0.21 AFM	0.16 AFM	0.13 AFM
J_3 (meV) Fe-Fe out of plane	0.00002 AFM	0.00003 AFM	0.00005 AFM

magnetic Hamiltonian is considered as follows:

$$H = J_1 \sum_{\langle i,j \rangle} S_i \cdot S_j + J_2 \sum_{\langle i,k \rangle} S_i \cdot S_k + J_3 \sum_{\langle i,l \rangle} S_i \cdot S_l + D \sum_i \left(S_i^z\right)^2,$$

(1)

where, S_i are the quantum spin operators, J_1 and J_2 are the nearest neighbor exchange interactions within 2D triangular lattice in the *ab* plane, and J_3 is the interlayer exchange interaction between two Fe^{3+} ions from two adjacent layers. The fourth term represents the contribution of single ion anisotropy. The anisotropy parameter D defines the strength of the single ion anisotropy which causes a small spin gap in the experimental INS spectra [Fig. 5(e)]. The collinear AFM structure, determined from the diffraction study [Fig. 4(c)], has been considered for the spin-wave calculations. The powder averaged spin-wave spectrum is calculated by considering the instrumental resolution, and magnetic form factor for the Fe^{3+} ions. It has been found that the relative strength of the exchange interactions J_1, and J_2 is proportional to the widths of the excitation modes (over ~ 0.25–2.0 and ~ 3.0–5.5 meV). The spin-wave simulations considering a variation of the J_1 values (keeping J_2 fixed) lead to a change in the energy value for the higher excitation band (Fig. 6). On the other hand, the variation of the J_2 value (keeping J_1 fixed) leads to a change in the energy ranges of both the higher and lower energy bands. With the decrease of the ratio (J_1/J_2) of the two in-plane exchange interactions J_1 and J_2 (keeping the interplanar interaction, $J_3 = 0$), a reduction in the difference between the higher and lower energy bands is evident [left column of Fig. 6]. By suitable adjustment of the exchange interaction values, the best agreement is obtained for $J_1 = -0.31$ meV (FM) and $J_2 = 0.15$ meV (AFM), and $D = 0.02$ meV (Table III), and the simulated INS spectra is shown in Fig. 7(a). The spin-wave calculated spectra (using the linear spin-wave theory) reproduce the energy ranges of the experimentally observed two dispersion modes over 0.25–2.0 and 3–5.5 meV nicely [Fig. 7(c)]. However, the theory estimates a much stronger intensity for the high energy mode (~ 3–5.5 meV) than that was measured experimentally. Such a discrepancy in the intensity of the higher energy mode could be due to the presence of magnon damping effect. The liner spin-wave theory, which considers a one magnon process, does not account for any magnon damping effect. Similar observations, i.e., the reduced intensity of the higher energy modes (magnon damping) was reported recently for several quantum magnets, $Na_3Co_2SbO_6$, $Na_2Co_2TeO_6$, and

α-$RuCl_3$ [63]. The magnon damping was correlated to the two-magnon process [63] where the two-magnon density of states overlap all over the upper mode of the single magnon, resulting in a strong magnon damping in the high energy spectra. For the studied compound $Na_3Fe(PO_4)_2$, the presence of two-magnon process was reported by the NMR study [35]. Therefore, the reduced intensity of the high-energy magnon mode (~ 3–5.5 meV) may be assigned to the two-magnon process induced damping of the one-magnon mode [Fig. 5(a)]. Any quantification of such a damping effect needs single crystal inelastic neutron scattering measurements along with a nonlinear spin wave theory analysis.

The signs of the derived in-plane magnetic exchange interactions are compatible with the second condition for the collinear stripy AFM ground state, i.e., with the different signs of the exchange interaction J_1 and J_2. The determined exchange interaction values from the INS are in good agreement with that derived from the DFT calculations (discussed later). It should be pointed out here that such opposing signs for J_1 and J_2 is unexpected given the relatively small distortion of the triangular lattice in this case (side lengths of 5.030 Å and 5.180 Å, respectively) with almost identical exchange interaction pathways (Table II). The mechanism for such unusual exchange interactions is discussed in the next section. Here, we would like to mention that although the values of the in-plane exchange interactions (J_1 and J_2) could be estimated from INS spectra, the interplanar exchange interaction (J_3) could not be estimated due to its very small value. Due to the large spacing between the magnetic layers (~ 6.91 Å), the interlayer exchange interaction (J_3) is expected to be very weak (few orders of magnitude weaker than J_1 and J_2), which is expected for such 2D-layered magnetic systems. The measured powder INS spectra is insensitive to such a weak exchange interaction value. Hence, it was not possible to estimate accurately such a weak interlayer exchange interaction (J_3) from the present INS data. Nevertheless, we have estimated the value of J_3 from the DFT calculations (presented in the next section).

C. Theoretical DFT calculations

To get further insight into the microscopic exchange interaction model, we have employed DFT calculations. The purpose of the DFT calculation is twofold. The primary purpose is to verify the signs and values of exchange interaction constants (J_1 and J_2) provided by the INS study, as well as
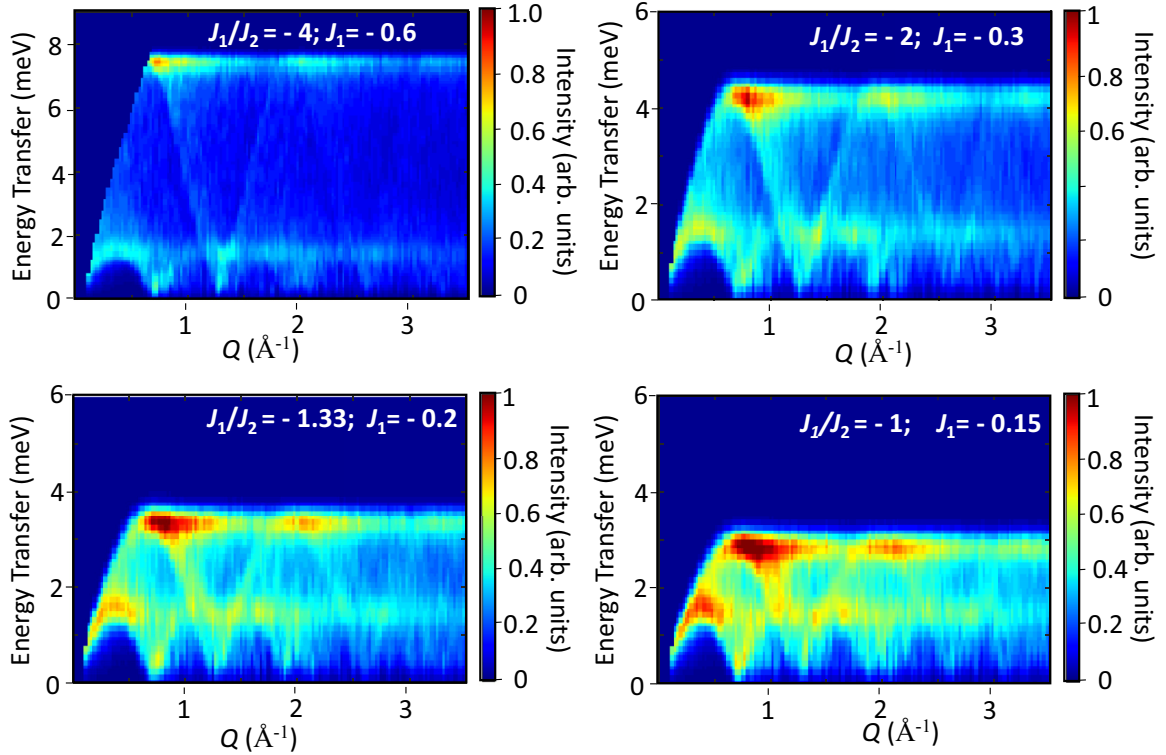
FIG. 6. Simulated spin-wave excitation spectra (using "*SpinW*" program) depending on the relative strengths of the exchange interactions (J_1/J_2) as per the triangular lattice model [spin-Hamiltonian given in Eq. (1)], keeping the interplanar interaction, $J_3 = 0$. The calculated spin-wave pattern is powder averaged, convoluted with the instrumental resolution, and corrected for the Fe^{3+} magnetic form factor.

to estimate of the strength of the weak interplanar exchange interaction J_3. The second purpose is to determine the mechanism of the magnetic exchange interaction, i.e., identifying the orbital contributions to the magnetic exchange interactions. The results obtained from the DFT calculations are discussed below.

1. Electronic structure

The calculated density of states (DOS) of $Na_3Fe(PO_4)_2$ are shown in Fig. 8. The Na and P states lie far above the Fermi level (E_f) and are in inert configuration in Na^+ and P^{5+} valence states, respectively. It is noted that in the absence of spin polarization, the density of states shows a metallic character, while the spin-polarized calculations within the GGA, assuming small Coulomb correlation at the $3d$ (Fe) site, provide the insulating solution. To study the effect of Coulomb U, on the electronic structure we systematically check U_{eff}^{Fe} value over 0–5 eV. The band gap and magnetic moments at the Fe site [$4.04\,\mu_B$ ($U_{eff}^{Fe} = 0\,eV$) to $4.38\,\mu_B$ ($U_{eff}^{Fe} = 5\,eV$)] increase with the increasing value of U. Therefore, the orbital occupancies and spin states remain unaffected. The Fe-$3d$ states are completely filled in the majority spin channel and completely empty in the minority spin channel. The oxygen atoms can be separated into two distinct categories based on the layered crystal structure. The category-I oxygen atoms lie in the ab plane, and connect the FeO_6 octahedra with the neighboring PO_4 tetrahedra. The category-II oxygen atoms are situated between two such magnetic layers. The difference in the density of states between these two sets of oxygen atoms

can be visualized in Fig. 8. A good overlap of the Fe$-3d$ density of states with the first set of oxygen atoms has been found. This also impacts the magnetic moment. While the former has a magnetic moment of $0.08\,\mu_B$ per site, the latter has a negligible value of $0.02\,\mu_B$. From the density of states and calculated magnetic moments, we conclude that Fe ions are in the $+3(3d^5)$ electronic state with high spin, $S = 5/2$. The Fe ions are the magnetically active site of the compound. The absence of overlap of the Fe-$3d$ with Na states or the states of the category-II oxygen atoms (as described previously) further suggests that this system is a magnetically 2D compound with negligible exchange interaction between the magnetic layers.

2. Magnetic exchange interactions

There are various ways to compute exchange interactions. In the present study, exchange interactions are estimated by mapping the DFT total energy of various possible spin configurations of the system on the effective Ising model [64], i.e., $E^{tot} = \sum_{ij} J_{ij} S_i^z S_j^z$, where J_{ij} is the magnetic exchange interaction between the ith and j^{th} sites and S_i^z and S_j^z are the effective spins at the corresponding sites (inset of Fig. 8). This methodology gives an estimation of the value and nature of the magnetic exchange interactions reasonable enough to explain the physical picture of the various classes of materials, although it is associated with a few limitations such as the need to choose the correct spin configurations, exchange path, and exchange-correlation functional [64–67]. We constructed a $1 \times 2 \times 1$ supercell of the crystal unit cell as shown in
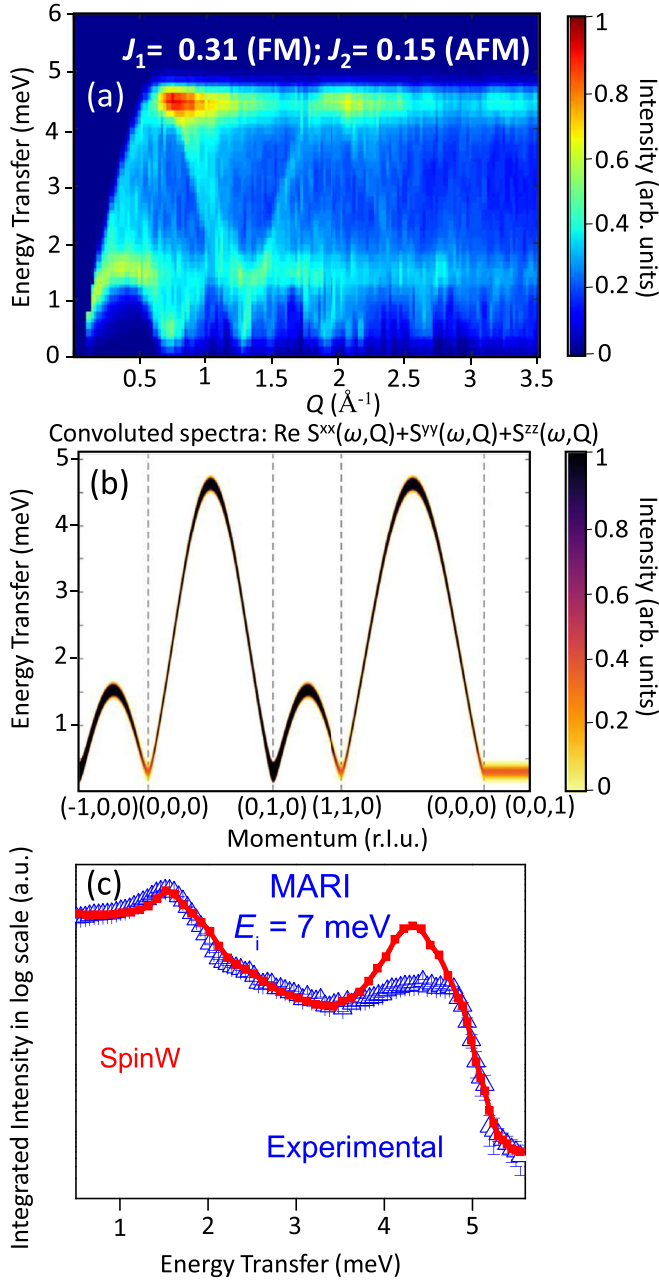
FIG. 7. (a) The theoretical powder averaged spin-wave spectrum as per the distorted TLAFM spin-Hamiltonian [Eq. (1)], using the best-fit parameters $J_1 = -0.31$ (FM) and $J_2 = 0.15$ (AFM). (b) The simulated dispersion curve along the different crystallographic directions. The intensity variation of the dispersion patterns shown by the color map. (c) Comparative plot between the experimental and the simulated integrated intensity vs energy transfer curves. The intensities were obtained by integration over $|Q| \sim 0-3\,\text{Å}^{-1}$ for the incident energy 7 meV. The blue scattered points represent the experimentally observed data and the red solid lines are the calculated patterns considering the as mentioned models.

FIG. 8. Projected density of states with $U^{Fe} = 5$ eV. The Fe-d states are represented by red. O-p states are represented by turquoise and orange. The turquoise DOS represents category-I oxygen atoms that are bonded with Fe and P atoms within the *ab* plane. The orange DOS refers to the category-II oxygen atoms that lie between the magnetic planes. The Fermi energy is set at zero in the energy scale. The inset shows magnetic spin configuration having lowest ground state energy obtained from DFT calculations.

Fig. 2(d). The supercell consists of eight Fe atoms and a total of 112 atoms. For our calculations, we have considered 10 possible spin configurations and constructed algebraic equations based on the Ising model. These were further solved simultaneously to obtain th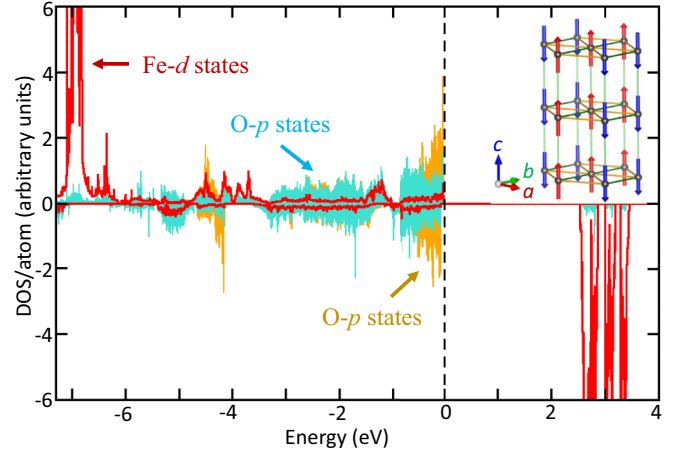e values and nature of exchange interaction J's. Table III shows the estimated values of exchange interactions J_1, J_2 and J_3, for three values of U_{eff} (= 4, 5, and 6 eV). As expected, with the increase in the value of U_{eff}^{Fe} we find a gradual decrease in value of exchange interaction J's. Furthermore, the values of the Fe-Fe out of plane exchange interactions are almost negligible (in the order of 10^{-5} meV) as compared to the in-plane Fe-Fe interactions. Among the three sets of the exchange interaction values obtained for $U_{eff}^{Fe} = 4$, 5, and 6 eV, the exchange interaction values [$J_1 = -0.33$ meV (FM) and $J_2 = 0.16$ meV (AFM)] for $U_{eff}^{Fe} = 5$ eV are found to be in good agreement with the exchange interaction values derived from the spin-wave analysis of the experimental INS spectra. The regenerated INS spectra for the set of exchange interaction values $J_1 = -0.33$ meV (FM) and $J_2 = 0.16$ meV (AFM), and $J_3 = 0.00003$ meV (AFM); reveal an excellent agreement with the experimentally observed features of INS spectra (Fig. 9). For the studied distorted TLAFM Na$_3$Fe(PO$_4$)$_2$, the value of the distortion parameter is thus $J_1/J_2 = -2$. The interaction parameters derived from both the spin-wave calculation and the DFT analysis, as detailed in Table III, successfully reproduce the magnetic structure unveiled by neutron powder diffraction. The DFT calculations reveal that the lowest energy magnetic structure is identical to that derived from the NPD analyses. Thus, the derived values of the exchange interactions allow us to establish the microscopic origin of the ordered collinear stripy AFM ground state as the FM J_1 and AFM J_2; and verify the theoretical magnetic phase diagram for a distorted TLAFM system as a function of distortion parameter J_1/J_2.

The above trend of exchange interactions can be better visualized by using the Wannier functions (Fig. 10) which provides the hopping integrals to neighboring Fe ions. It also explains the role of the intermediate O and P ions on exchange interactions. The central part of the Wannier functions
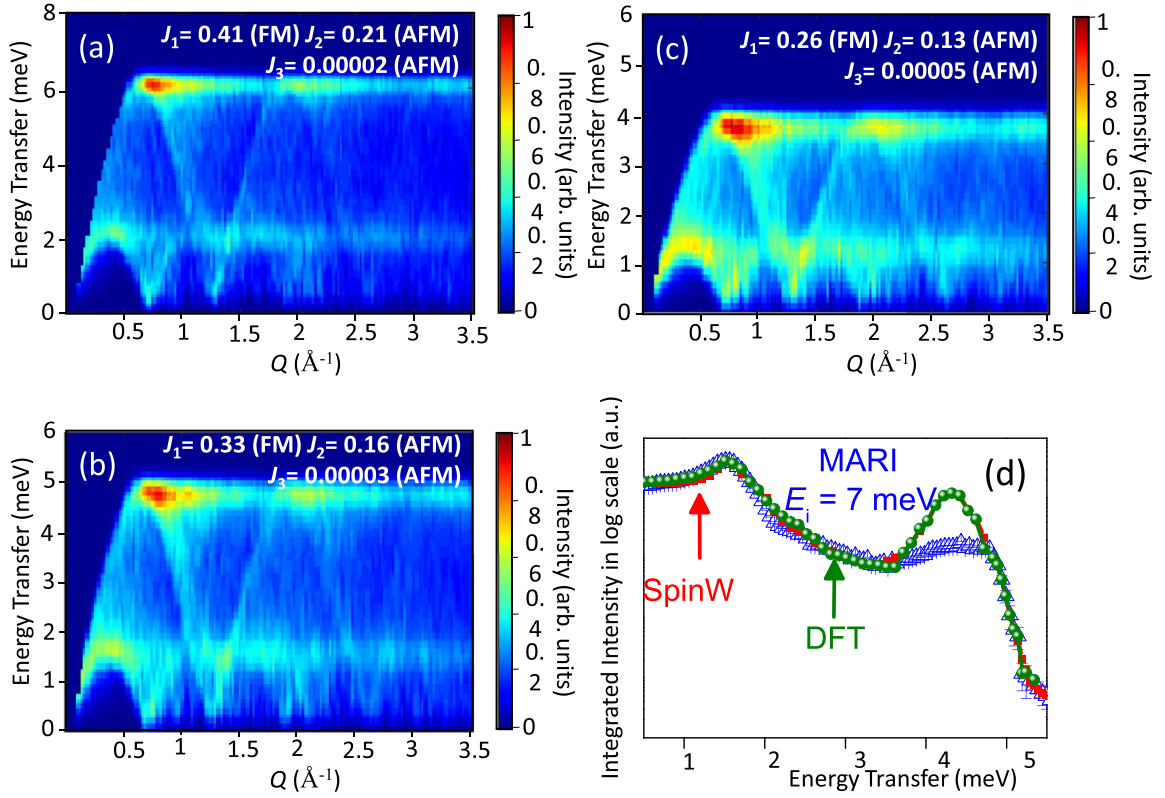
FIG. 9. The simulated INS spectra by considering the three sets of exchange interaction values (a) $J_1 = -0.41$ (FM), $J_2 = 0.21$ (AFM) and $J_3 = 0.00002$ (AFM); (b) $J_1 = -0.33$ (FM), $J_2 = 0.16$ (AFM) and $J_3 = 0.00003$ (AFM) and (c) $J_1 = -0.26$ (FM), $J_2 = 0.13$ (AFM) and $J_3 = 0.00005$ (AFM) obtained from DFT calculations (Table III). (d) Comparison between experimental curves with the same obtained from spin wave [Figs. 7(c) and 7(d)] and DFT [Fig. 9(b)] calculations. The blue scattered points represent the experimentally observed data, red and green solid lines are the calculated patterns obtained from the simulation of the spin wave calculations and the output of DFT results, respectively. The experimental intensities were obtained by integration over $|Q| \sim 0-3\,\text{Å}^{-1}$ for the incident energy 7 meV.

is shaped according to the plotted Fe-3d character, whereas the tails situated at other atoms show the effect of the orbitals which was renormalized. The weight of the tails at neighboring atoms dictates the strength of the exchange interaction
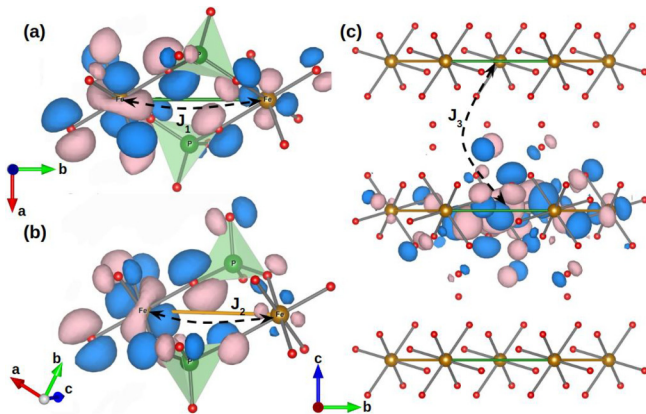

FIG. 10. Wannier functions of Fe-3d_{xy}, centered at Fe site. The exchange interactions J_1, J_2 and J_3 are shown in (a), (b), and (c), respectively. Pink and blue color lobes represent isosurfaces with positive and negative signs, respectively. The orange and red spheres correspond to Fe and O atoms, respectively.

between the connected atomic sites. From the plot it is clear that the path from one Fe to another Fe is via Fe-O-O-Fe, without going via P. This is true for both exchange interactions J_1 and J_2. Oxygen 2p orbital has a very strong role in this superexchange interaction. However, the phosphorus ions are in +5 state (having inert [Ne] configuration) and does not have any contribution on the superexchange interactions. Figure 10(a) shows the Fe-3d_{xy} as projected in the x-y plane, whereas, Fig. 10(b) shows the same orbital as projected in the y-z plane. From the central part of Fe-3d_{xy} we can see that the strength of the in-plane interaction J_1 is comparatively stronger than that for J_2. At the same time Fig. 10(c) shows that the out-of-plane exchange interaction J_3 is negligible.

In the present study, involving experimental neutron scattering and DFT calculations, we have shown the realization of the noteworthy feature of nearly perfect 2D magnetic lattice in Na$_3$Fe(PO$_4$)$_2$ with a negligible interplanar coupling ($|J_3/J_1| = 9 \times 10^{-5}$). This is one of the most perfect 2D triangular lattice reported so far, and comparable to several other classical examples of TLAFMs VX_2 with $X = $ Cl and Br and ABX_3-type compounds, where, $A = $ Cs and Rb, $B = $ Mn, Cu, Ni, and Co, and $X = $ Cl, Br, and I [68], providing an opportunity to study the triangular lattice phase diagram without an influence of interplanar effect. The

presence of interlayer exchange interactions often modifies the magnetic ground state qualitatively as reported for several compounds [29,69–71]. The present compound $Na_3Fe(PO_4)_2$ is also one of the rare examples of triangular lattice having collinear stripy AFM state that is appearing from the FM J_1 and AFM J_2, i.e., with a -ve ratio of J_1/J_2. In all other cases, the stripy AFM state appears from the competing AFM interactions with a +ve ratio of J_1/J_2. We have shown in the present study that the FM J_1 and AFM J_2, rarely expected for a triangular lattice having equivalent exchange pathways Fe-O-O-Fe with almost similar side lengths (5.030 Å and 5.180 Å), are realizable through comprehensive neutron scattering and DFT studies. This also reveal the necessity of such a microscopic study to realize the true nature of the Hamiltonian and the origin of the observed magnetic properties. Further, the observed weak easy axis single-ion anisotropy in $Na_3Fe(PO_4)_2$ is in favor of the collinear AFM state [72,73] as compared to the easy-plane anisotropy which favors toward a chiral 120° ground state [19]. A previous report demonstrated spin-wave excitations of the single crystal spin-5/2 type-II distorted TLAFM $Ba_3MnSb_2O_9$ [31]. The INS spectra and the analysis of the spin-wave excitations revealed small easy-plane anisotropy which favors the in-plane noncollinear 120° chiral state. Thus, it can be stated that anisotropy also plays a crucial role in dictating the magnetic ground state.

It is noteworthy that the derived in-plane magnetic exchange interactions FM J_1 and AFM J_2 from both INS study and DFT calculations indicate an AFM ground state, as the numbers of the AFM J_2 exchange interaction bonds (4 Nos.) are higher than the FM J_1 exchange bonds (3 Nos.) within the *ab* planes. Thus, an effective AFM ordering is expected, and this is consistent with the experimental bulk magnetization data (Fig. 3) revealing an antiferromagnetic transition with $T_N \sim 10.8$ K as well as neutron diffraction data revealing an AFM ordered ground state (Fig. 4). Further, the Curie-Weiss temperature (θ_{CW}) ~ -37.01 K of $Na_3Fe(PO_4)_2$ is consistent with the exchange interaction values [36]. As per the mean-field theory, the Curie-Wiess temperature and the exchange interaction are related by the expression $\theta_{CW} = -[zJS(S+1)]/3k_B$, where, $z = 6$ is the coordination number. The calculated θ_{CW} value for the AFM exchange interaction $J_2 = 0.16$ meV (as determined in the present study) is $= -33$ K, which closely matches with the θ_{CW}, derived from the magnetic susceptibility data.

Now we compare the magnetic properties of $Na_3Fe(PO_4)_2$ with the other members of the triangular lattice compounds $RA'_2X(YO_4)_2$ (where, R = Na, K, Rb, Ag; A' = Na$_2$ and Ag$_2$, X = Cr, Fe; and Y = P, V) [1,74–78]. Among them, the compound $Ag_3Cr(VO_4)_2$ having isosceles type-I distortion in a triangular lattice, possesses a long-range collinear stripy AFM ground state as like the studied compound $Na_3Fe(PO_4)_2$. In contrast, the compounds $AAg_2Cr(VO_4)_2$ (A = Rb, K) having uniform triangular lattices, do not show any long-range magnetic order [29]. Further, the Fe-based compound $KFe(MoO_4)_2$ having isosceles type-II distortion in triangular lattice, also exhibits a long-range collinear stripy AFM ground state, as observed for the studied compound $Na_3Fe(PO_4)_2$. On the other hand, $RbFe(MoO_4)_2$ having uniform triangular lattices, is found to exhibit 120° chiral ground state

[29]. Furthermore, the superexchange interactions between the Fe ions via the linkers, $(PO_4)^{3-}$ phosphates and $(VO_4)^{3-}$ vanadates play an important role on the magnetic properties. It has been reported that the distance between the oxygen ions for superexchange interactions via vanadates is 0.4 Å larger than the superexchange interactions via phosphates. This reduces the effective overlap and consequently leads to the smaller exchange interaction values. Furthermore, the strength as well as sign of the superexchange interactions between the Fe ions also depend on the relative orientation of the tetrahedral $(PO_4)^{3-}$ phosphates or $(VO_4)^{3-}$ vanadates to the transition metal centered octahedra, as observed for $AAg_2M[VO_4]_2$ (A = Ba, Sr; M = Co, Ni, Cu) compounds [75]. For example, in the case of $BaAg_2Cu[VO_4]_2$, it has been reported that a change in the relative orientations of $[MO_6]$ and $[VO_4]$ from ~130° to ~100° leads to a FM to AFM effective superexchange interactions. For the studied compound $Na_3Fe(PO_4)_2$, the average relative orientations of $[FeO_6]$ and $[PO_4]$ have been found to be ~140.6° and ~92.09° along the superexchange pathways J_1 and J_2, respectively. This is consistent with the effective superexchange interactions FM J_1 and AFM J_2, as obtained from the experimental INS and DFT calculations. Hence, it is imperative to understand the significance of linkers, specifically $(PO_4)^{3-}$ phosphates or $(VO_4)^{3-}$ vanadates, as a crucial tuning parameter to assess the different types of distorted TLAFM. Further, our DFT study on the present compound $Na_3Fe(PO_4)_2$ reveals that the superexchange interactions (J_1 and J_2) occur via Fe-O-O-Fe. The present understandings are, thus, directly extensible to the series of TLAFM compounds $RA'_2X(YO_4)_2$ to shed light on their magnetic properties and understanding the magnetic phase diagram (Fig. 1) in general. The present study provides the pathway for understanding of the microscopic Hamiltonians of TLAFM in general [29], and establishes the mechanism of exchange interactions in establishing the magnetism of distorted isosceles J_1-J_2 TLAFM.

IV. SUMMARY AND CONCLUSIONS

In summary, we have determined magnetic ground state and spin Hamiltonian of the distorted TLAFM system $Na_3Fe(PO_4)_2$ by a combined study of experimental neutron scattering and theoretical DFT calculations. The magnetic ordering of the distorted 2D-triangular lattice compound $Na_3Fe(PO_4)_2$ is characterized by dc/ac susceptibility, heat capacity, and low temperature neutron diffraction, which is consistent with the earlier report [38]. Neutron diffraction study reveals an ordered collinear stripy AFM ground state. The magnetic excitation spectra, studied by INS, consist of two band of magnetic scattering over 0.25–2.0 and 3.0–5.5 meV. The spin Hamiltonian of $Na_3Fe(PO_4)_2$, determined from both the experimentally observed INS spectra and theoretical DFT calculations, reveal dominating 2D exchange interactions within the triangular layers with a negligible interlayer interaction. The NN exchange interactions within the triangular lattice consist of two exchange constants with different signs and strengths viz., $J_1 = -0.33$ meV (FM) and $J_2 = 0.16$ meV (AFM). The precisely determined values of exchange interactions allows us to shed light on the microscopic

origin of the observed collinear stripy AFM state and verify the theoretically predicted magnetic phase diagram for a distorted TLAFM system. Further, the Wannier function (DFT) calculations demonstrate the mechanism of the exchange interactions between the Fe ions which reveal the exchange interactions occur through Fe-O-O-Fe pathways, without going via P^{+5} ions (having inert [Ne] configuration). The present study, therefore, provides an insight of the spin-spin correlations, spin-Hamiltonian, and exchange mechanism of $Na_3Fe(PO_4)_2$, and verify the theoretical magnetic phase diagram for a distorted TLAFM system.

[1] N. E. Amuneke, D. E. Gheorghe, B. Lorenz, and A. Möller, Synthesis, crystal structure, and physical properties of $BaAg_2Cu[VO_4]_2$: A new member of the S = 1/2 triangular lattice, Inorg. Chem. **50**, 2207 (2011).

[2] T. Giamarchi, *Quantum Physics in One Dimension* (Clarendon, Oxford, 2003).

[3] R. Moessner and A. P. Ramirez, Geometrical frustration, Phys. Today **59**, 24 (2006).

[4] B. Saha, A. K. Bera, S. M. Yusuf, and A. Hoser, Two-dimensional short-range spin-spin correlations in the layered spin-3/2 maple leaf lattice antiferromagnet $Na_2Mn_3O_7$ with crystal stacking disorder, Phys. Rev. B **107**, 064419 (2023).

[5] B. Bernu, P. Lecheminant, C. Lhuillier, and L. Pierre, Exact spectra, spin susceptibilities, and order parameter of the quantum Heisenberg antiferromagnet on the triangular lattice, Phys. Rev. B **50**, 10048 (1994).

[6] L. Capriotti, A. E. Trumper, and S. Sorella, Long-range Néel order in the triangular Heisenberg model, Phys. Rev. Lett. **82**, 3899 (1999).

[7] A. Chernyshev and M. Zhitomirsky, Spin waves in a triangular lattice antiferromagnet: Decays, spectrum renormalization, and singularities, Phys. Rev. B **79**, 144416 (2009).

[8] S. Fujiki and D. D. Betts, High temperature series expansion of the fluctuation of the vector chirality for the spin-1/2 XY antiferromagnet on the triangular lattice, J. Phys. Soc. Jpn. **60**, 435 (1991).

[9] T. Jolicoeur and J. C. Le Guillou, Spin-wave results for the triangular Heisenberg antiferromagnet, Phys. Rev. B **40**, 2727 (1989).

[10] E. A. Zvereva, I. A. Presniakov, M.-H. Whangbo, H.-J. Koo, T. V. Frantsuzenko, O. A. Savelieva, A. V. Sobolev, V. B. Nalbandyan, P.-S. Shih, and J.-C. Chiang, Crucial role of site disorder and frustration in unusual magnetic properties of quasi-2D triangular lattice antimonate Na_4FeSbO_6, Appl. Magn. Reson. **46**, 1121 (2015).

[11] B. Bernu, C. Lhuillier, and L. Pierre, Signature of Néel order in exact spectra of quantum antiferromagnets on finite lattices, Phys. Rev. Lett. **69**, 2590 (1992).

[12] Y. Doi, Y. Hinatsu, and K. Ohoyama, Structural and magnetic properties of pseudo-two-dimensional triangular antiferromagnets $Ba_3MSb_2O_9$ (M = Mn, Co, and Ni), J. Phys. Condens. Matter **16**, 8923 (2004).

[13] T. Inami, Y. Ajiro, and T. Goto, Magnetization process of the triangular lattice antiferromagnets, $RbFe(MoO_4)_2$ and $CsFe(SO_4)_2$, J. Phys. Soc. Jpn. **65**, 2374 (1996).

[14] H. Serrano-González, S. Bramwell, K. Harris, B. Kariuki, L. Nixon, I. Parkin, and C. Ritter, Magnetic structures of the triangular lattice magnets $AFe(SO_4)_2$ (A = K, Rb, Cs), J. Appl. Phys. **83**, 6314, (1998).

[15] T. Inami, Neutron powder diffraction experiments on the layered triangular-lattice antiferromagnets $RbFe(MoO_4)_2$ and $CsFe(SO_4)_2$, J. Solid State Chem. **180**, 2075 (2007).

[16] A. Smirnov, L. Svistov, L. Prozorova, A. Zheludev, M. Lumsden, E. Ressouche, O. Petrenko, K. Nishikawa, S. Kimura, M. Hagiwara *et al.*, Chiral and collinear ordering in a distorted triangular antiferromagnet, Phys. Rev. Lett. **102**, 037202 (2009).

[17] R. Ishii, S. Tanaka, K. Onuma, Y. Nambu, M. Tokunaga, T. Sakakibara, N. Kawashima, Y. Maeno, C. Broholm, and D. P. Gautreaux, Successive phase transitions and phase diagrams for the quasi-two-dimensional easy-axis triangular antiferromagnet $Rb_4Mn(MoO_4)_3$, Europhys. Lett. **94**, 17001 (2011).

[18] S. Ito, N. Kurita, H. Tanaka, S. Ohira-Kawamura, K. Nakajima, S. Itoh, K. Kuwahara, and K. Kakurai, Structure of the magnetic excitations in the spin-1/2 triangular-lattice Heisenberg antiferromagnet $BaCoSb_2O_9$, Nat. Commun. **8**, 235 (2017).

[19] R. Rawl, L. Ge, Z. Lu, Z. Evenson, C. D. Cruz, Q. Huang, M. Lee, E. Choi, M. Mourigal, and H. Zhou, $Ba_8MnNb_6O_{24}$: A model two-dimensional spin-5/2 triangular lattice antiferromagnet, Phys. Rev. Mater. **3**, 054412 (2019).

[20] R. Clark and W. Moulton, Cs^{133} and Cl^{35} NMR in Antiferromagnetic $CsNiCl_3$, Phys. Rev. B **5**, 788 (1972).

[21] A. Harrison, M. Collins, J. Abu-Dayyeh, and C. Stager, Magnetic structures and excitations of $CsMnI_3$: A one-dimensional Heisenberg antiferromagnet with easy-axis anisotropy, Phys. Rev. B **43**, 679 (1991).

[22] M. Lee, E. Choi, X. Huang, J. Ma, C. D. Cruz, M. Matsuda, W. Tian, Z. Dun, S. Dong, and H. Zhou, Magnetic phase diagram and multiferroicity of $Ba_3MnNb_2O_9$: A spin-5/2 triangular lattice antiferromagnet with weak easy-axis anisotropy, Phys. Rev. B **90**, 224402 (2014).

[23] M. Lee, J. Hwang, E. Choi, J. Ma, C. D. Cruz, M. Zhu, X. Ke, Z. Dun, and H. Zhou, Series of phase transitions and multiferroicity in the quasi-two-dimensional spin-1/2 triangular-lattice antiferromagnet $Ba_3CoNb_2O_9$, Phys. Rev. B **89**, 104420 (2014).

[24] P.-É. Melchy and M. Zhitomirsky, Interplay of anisotropy and frustration: Triple transitions in a triangular-lattice antiferromagnet, Phys. Rev. B **80**, 064411 (2009).

[25] A. Albaalbaky, Y. Kvashnin, R. Patte, and D. Ledue, Analytical and numerical investigations of noncollinear magnetic ordering

in the frustrated delafossite $CuCrO_2$, Phys. Rev. B **99**, 104415 (2019).

[26] J. Lou, A. W. Sandvik, and N. Kawashima, Antiferromagnetic to valence-bond-solid transitions in two-dimensional SU (N) Heisenberg models with multispin interactions, Phys. Rev. B **80**, 180414(R) (2009).

[27] Z. Lu, L. Ge, G. Wang, M. Russina, G. Günther, C. dela Cruz, R. Sinclair, H. Zhou, and J. Ma, Lattice distortion effects on the frustrated spin-1 triangular-antiferromagnet $A_3NiNb_2O_9$ (A = Ba, Sr, and Ca), Phys. Rev. B **98**, 094412 (2018).

[28] R. Tamura, S. Tanaka, and N. Kawashima, Second-order phase transition in the Heisenberg model on a triangular lattice with competing interactions, Phys. Rev. B **87**, 214401 (2013).

[29] J. Tapp, C. dela Cruz, M. Bratsch, N. Amuneke, L. Postulka, B. Wolf, M. Lang, H. Jeschke, R. Valentí, P. Lemmens, and A. Moller, From magnetic order to spin-liquid ground states on the S = 3/2 triangular lattice, Phys. Rev. B **96**, 064404 (2017).

[30] W. M. Zhang, W. M. Saslow, and M. Gabay, Row generalization of the fully frustrated triangular XY model, Phys. Rev. B **44**, 5129 (1991).

[31] M. Shu, W. Dong, J. Jiao, J. Wu, G. Lin, Y. Kamiya, T. Hong, H. Cao, M. Matsuda, W. Tian *et al.*, Static and dynamical properties of the spin-5/2 nearly ideal triangular lattice antiferromagnet $Ba_3MnSb_2O_9$, Phys. Rev. B **108**, 174424 (2023).

[32] D. Heidarian, S. Sorella, and F. Becca, Spin-$\frac{1}{2}$ Heisenberg model on the anisotropic triangular lattice: From magnetism to a one-dimensional spin liquid, Phys. Rev. B **80**, 012404 (2009).

[33] T. A. Soldatov, A. I. Smirnov, and A. V. Syromyatnikov, Spin dynamics in ordered phases of anisotropic triangular-lattice antiferromagnet Cs_2CoBr_4, Phys. Rev. B **108**, 184426 (2023).

[34] A. Zorko, O. Adamopoulos, M. Komelj, D. Arčon, and A. Lappas, Frustration-induced nanometre-scale inhomogeneity in a triangular antiferromagnet, Nat. Commun. **5**, 3222 (2014).

[35] D. V. Ambika, Q.-P. Ding, S. J. Sebastian, R. Nath, and Y. Furukawa, Static and dynamic magnetic properties of the spin-5/2 triangle lattice antiferromagnet $Na_3Fe(PO_4)_2$ studied by ^{31}P NMR, J. Phys.: Condens. Matter **35**, 015803 (2022).

[36] M. S. Belkhiria, S. Laaribi, A. B. H. Amara, and M. B. Amara, Structure of $Na_3Fe(PO_4)_2$ from powder X-ray dataAnalyse structurale de $Na_3Fe(PO_4)_2$ à partir des données de diffraction RX sur poudre, Annales de Chimie Science des Matériaux **23**, 117 (1998).

[37] V. Morozov, B. Lazoryak, A. Malakho, K. Pokholok, S. Polyakov, and T. Terekhina, The glaserite-like structure of double sodium and iron phosphate $Na_3Fe(PO_4)_2$, J. Solid State Chem. **160**, 377 (2001).

[38] S. J. Sebastian, S. S. Islam, A. Jain, S. M. Yusuf, M. Uhlarz, and R. Nath, Collinear order in the spin-5/2 triangular-lattice antiferromagnet $Na_3Fe(PO_4)_2$, Phys. Rev. B **105**, 104425 (2022).

[39] R. Salmon, C. Parent, G. Le Flem, M. Vlasse, and C. Chemistry, The crystal structure of the sodium erbium orthovanadate α-$Na_3Er(VO_4)_2$, Acta Crystallogr. B **32**, 2799 (1976).

[40] M. Vlasse, C. Parent, R. Salmon, G. Le Flem, and P. Hagenmuller, The structures of the $Na_0Ln(XO_4)_2$ phases (Ln = rare earth, X = P, V, As), J. Solid State Chem. **35**, 318 (1980).

[41] M. Vlasse, R. Salmon, and C. Parent, Crystal structure of sodium lanthanum orthovanadate, $Na_3La(VO_4)_2$, Inorg. Chem. **15**, 1440 (1976).

[42] M. Zhizhin, V. Morozov, A. Bobylev, A. Popov, F. Spiridonov, L. Komissarova, and B. Lazoryak, Structure of polymorphous

[43] modifications of double sodium and indium phosphate, J. Solid State Chem. **149**, 99 (2000).

[43] J. Rodríguez-Carvajal, Recent advances in magnetic structure determination by neutron powder diffraction, Physica B **192**, 55 (1993).

[44] A. Wills, Long-range ordering and representational analysis of the jarosites, Phys. Rev. B **63**, 064430 (2001).

[45] A. K. Bera, S. M. Yusuf, L. Keller, F. Yokaichiya, and J. R. Stewart, Magnetism of two-dimensional honeycomb layered $Na_2Ni_2TeO_6$ driven by intermediate Na-layer crystal structure, Phys. Rev. B **105**, 014410 (2022).

[46] A. K. Bera, S. M. Yusuf, A. Kumar, and C. Ritter, Zigzag antiferromagnetic ground state with anisotropic correlation lengths in the quasi-two-dimensional honeycomb lattice compound $Na_2Co_2TeO_6$, Phys. Rev. B **95**, 094424 (2017).

[47] O. Arnold, J.-C. Bilheux, J. Borreguero, A. Buts, S. I. Campbell, L. Chapon, M. Doucet, N. Draper, R. F. Leal, and M. Gigg, Mantid—Data analysis and visualization package for neutron scattering and μ SR experiments, Nucl. Instrum. Methods. Phys. Res. A **764**, 156 (2014).

[48] A. K. Bera, S. M. Yusuf, and D. T. Adroja, Excitations in the spin-1 trimer chain compound $CaNi_3P_4O_{14}$: From gapped dispersive spin waves to gapless magnetic excitations, Phys. Rev. B **97**, 224413 (2018).

[49] S. Toth and B. Lake, Linear spin wave theory for single-Q incommensurate magnetic structures, J. Phys. Condens. Matter **27**, 166002 (2015).

[50] G. Kresse and J. J. P. R. B. Furthmüller, Efficient iterative schemes for *ab initio* total-energy calculations using a plane-wave basis set, Phys. Rev. B **54**, 11169 (1996).

[51] G. Kresse and J. Hafner, *Ab initio* molecular dynamics for liquid metals, Phys. Rev. B **47**, 558 (1993).

[52] A. K. Bera, B. Lake, A. T. M. N. Islam, O. Janson, H. Rosner, A. Schneidewind, J. T. Park, E. Wheeler, and S. Zander, Consequences of critical interchain couplings and anisotropy on a Haldane chain, Phys. Rev. B **91**, 144414 (2015).

[53] J. P. Perdew, K. Burke, and M. Ernzerhof, Generalized gradient approximation made simple, Phys. Rev. Lett. **77**, 3865 (1996).

[54] V. I. Anisimov, I. Solovyev, M. Korotin, M. Czyżyk, and G. Sawatzky, Density-functional theory and NiO photoemission spectra, Phys. Rev. B **48**, 16929 (1993).

[55] S. L. Dudarev, G. A. Botton, S. Y. Savrasov, C. J. Humphreys, and A. P. Sutton, Electron-energy-loss spectra and the structural stability of nickel oxide: An LSDA+ U study, Phys. Rev. B **57**, 1505 (1998).

[56] A. A. Mostofi, J. R. Yates, Y.-S. Lee, I. Souza, D. Vanderbilt, and N. Marzari, Wannier90: A tool for obtaining maximally-localised Wannier functions, Comput. Phys. Commun. **178**, 685 (2008).

[57] R. Nikolova and V. Kostov-Kytin, Crystal chemistry of "glaserite" type compounds, Bulg. Chem. Commun. **45**, 418 (2013).

[58] M. Azhar and M. Mostovoy, Incommensurate spiral order from double-exchange interactions, Phys. Rev. Lett. **118**, 027203 (2017).

[59] J. T. Haraldsen, M. Swanson, G. Alvarez, and R. S. Fishman, Spin-wave instabilities and noncollinear magnetic phases of a geometrically frustrated triangular-lattice antiferromagnet, Phys. Rev. Lett. **102**, 237204 (2009).

[60] H. Kawamura, Commensurate and incommensurate helical orderings in stacked-triangular antiferromagnets: CsMnBr$_3$ and RbMnBr$_3$, Prog. Theor. Phys. Suppl. **101**, 545 (1990).

[61] E. Stiakakis, A. Wilk, J. Kohlbrecher, D. Vlassopoulos, and G. Petekidis, Slow dynamics, aging, and crystallization of multi-arm star glasses, Phys. Rev. E **81**, 020402(R) (2010).

[62] F. Ye, J. A. Fernandez-Baca, R. S. Fishman, Y. Ren, H. J. Kang, Y. Qiu, and T. Kimura, Magnetic interactions in the geometrically frustrated triangular lattice antiferromagnet CuFeO$_2$, Phys. Rev. Lett. **99**, 157201 (2007).

[63] C. Kim, J. Jeong, G. Lin, P. Park, T. Masuda, S. Asai, S. Itoh, H.-S. Kim, H. Zhou, and J. Ma, Antiferromagnetic Kitaev interaction in $J_{\text{eff}} = 1/2$ cobalt honeycomb materials Na$_3$Co$_2$SbO$_6$ and Na$_2$Co$_2$TeO$_6$, J. Phys. Condens. Matter **34**, 045802 (2021).

[64] V. Mazurenko, F. Mila, and V. Anisimov, Electronic structure and exchange interactions of Na$_2$V$_3$O$_7$, Phys. Rev. B **73**, 014418 (2006).

[65] S. Kanungo, B. Yan, M. Jansen, and C. Felser, *Ab initio* study of low-temperature magnetic properties of double perovskite Sr$_2$FeOsO$_6$, Phys. Rev. B **89**, 214414 (2014).

[66] B. E. Prasad, S. Sadhukhan, T. C. Hansen, C. Felser, S. Kanungo, and M. Jansen, Synthesis, crystal and magnetic structure of the spin-chain compound Ag$_2$RuO$_4$, Phys. Rev. Mater. **4**, 024418 (2020).

[67] J. Sannigrahi, J. Sichelschmidt, B. Koo, A. Banerjee, S. Majumdar, and S. Kanungo, Microscopic investigation of low dimensional magnet Sc$_2$Cu$_2$O$_5$: Combined experimental and *ab initio* approach, J. Phys. Condens. Matter **31**, 245802 (2019).

[68] A. Du, J. Li, and G. Z. Wei, The Heisenberg model on a stacked-triangular lattice: Spin green function approach, Phys. Status Solidi B **240**, 230 (2003).

[69] H. Kadowaki, H. Kikuchi, and Y. Ajiro, Neutron powder diffraction study of the two-dimensional triangular lattice antiferromagnet CuCrO$_2$, J. Phys. Condens. Matter **2**, 4485 (1990).

[70] M. Poienar, F. Damay, C. Martin, V. Hardy, A. Maignan, and G. André, Structural and magnetic properties of CuCr$_{1-x}$Mg$_x$O$_2$ by neutron powder diffraction, Phys. Rev. B **79**, 014412 (2009).

[71] M. Poienar, F. Damay, C. Martin, J. Robert, and S. Petit, Spin dynamics in the geometrically frustrated multiferroic CuCrO$_2$, Phys. Rev. B **81**, 104411 (2010).

[72] E. Wawrzyńska, R. Coldea, E. M. Wheeler, I. I. Mazin, M. D. Johannes, T. Sörgel, M. Jansen, R. M. Ibberson, and P. G. Radaelli, Orbital degeneracy removed by charge order in triangular antiferromagnet AgNiO$_2$, Phys. Rev. Lett. **99**, 157204 (2007).

[73] E. M. Wheeler, R. Coldea, E. Wawrzyńska, T. Sörgel, M. Jansen, M. M. Koza, J. Taylor, P. Adroguer, and N. Shannon, Spin dynamics of the frustrated easy-axis triangular antiferromagnet 2H-AgNiO$_2$ explored by inelastic neutron scattering, Phys. Rev. B **79**, 104421 (2009).

[74] S. Lee, R. Klauer, J. Menten, W. Lee, S. Yoon, H. Luetkens, P. Lemmens, A. Möller, and K.-Y. Choi, Unconventional spin excitations in the S = 3 2 triangular antiferromagnet RbAg$_2$Cr[VO$_4$]$_2$, Phys. Rev. B **101**, 224420 (2020).

[75] A. Möller, N. E. Amuneke, P. Daniel, B. Lorenz, R. Clarina, M. Gooch, and P. C. Chu, AAg$_2$M[VO$_4$]$_2$ (A = Ba, Sr; M = Co, Ni): A series of ferromagnetic insulators, Phys. Rev. B **85**, 214422 (2012).

[76] G. Nakayama, S. Hara, H. Sato, Y. Narumi, and H. Nojiri, Synthesis and magnetic properties of a new series of triangular-lattice magnets, Na$_2$BaMV$_2$O$_8$ (M = Ni, Co, and Mn), J. Phys. Condens. Matter **25**, 116003 (2013).

[77] S. J. Sebastian, K. Somesh, M. Nandi, N. Ahmed, P. Bag, M. Baenitz, B. Koo, J. Sichelschmidt, A. A. Tsirlin, Y. Furukawa, and R. Nath, Quasi-one-dimensional magnetism in the spin-1/2 antiferromagnet BaNa$_2$Cu(VO$_4$)$_2$, Phys. Rev. B **103**, 064413 (2021).

[78] A. A. Tsirlin, A. Möller, B. Lorenz, Y. Skourski, and H. Rosner, Superposition of ferromagnetic and antiferromagnetic spin chains in the quantum magnet BaAg$_2$Cu[VO$_4$]$_2$, Phys. Rev. B **85**, 014401 (2012).